



# Negative edges and soft thresholding in complex network analysis of resting state functional connectivity data

Adam J. Schwarz<sup>a,\*</sup>, John McGonigle<sup>b</sup>

<sup>a</sup> Department of Psychological and Brain Sciences, Indiana University, 1101 E. 10th Street, Bloomington, IN 47405, USA

<sup>b</sup> Psychopharmacology Unit, University of Bristol, Bristol, BS8 1UB, UK

## ARTICLE INFO

### Article history:

Received 9 October 2010

Revised 23 November 2010

Accepted 16 December 2010

Available online 29 December 2010

### Keywords:

Functional connectivity

Graph theory

Resting state

Weighted networks

Soft-thresholding

Reproducibility

## ABSTRACT

Complex network analyses of functional connectivity have consistently revealed non-random (modular, small-world, scale-free-like) behavior of hard-thresholded networks constructed from the right-tail of the similarity histogram. In the present study we determined network properties resulting from edges constrained to specific ranges across the full correlation histogram, in particular the left (negative-most) tail, and their dependence on the confound signal removal strategy employed. In the absence of global signal correction, left-tail networks comprised predominantly long range connections associated with weak correlations and were characterized by substantially reduced modularity and clustering, negative assortativity and  $\gamma < 1$ . Deconvolution of specific confound signals (white matter, CSF and motion) resulted in the most robust within-subject reproducibility of global network parameters (ICCs ~0.5). Global signal removal altered the network topology in the left tail, with the clustering coefficient and assortativity converging to zero. Networks constructed from the absolute value of the correlation coefficient were thus compromised following global signal removal since the different right-tail and left-tail topologies were mixed. These findings informed the construction of soft-thresholded networks, replacing the hard thresholding or binarization operation with a continuous mapping of all correlation values to edge weights, suppressing rather than removing weaker connections and avoiding issues related to network fragmentation. A power law adjacency function with  $\beta = 12$  yielded modular networks whose parameters agreed well with corresponding hard-thresholded values, that were reproducible in repeated sessions across many months and evidenced small-world-like and scale-free-like properties.

© 2010 Elsevier Inc. All rights reserved.

## Introduction

Functional connectivity analyses of neuroimaging data are based on the concept of synchrony between the signal responses in spatially distinct brain regions (Biswal et al., 1995). In particular, the analysis of temporal correlations between low-frequency ( $\sim 0.01 < f < 0.1$  Hz) oscillations in task-free (“resting state”) blood oxygenation-level dependent functional MRI (BOLD fMRI) data has revealed a rich spatiotemporal structure that has become a dominant theme in brain imaging and neuroscience (Fox and Raichle, 2007; Beckmann et al., 2005). The brain's functional correlation structure has been shown to correlate with electrophysiological signatures (Mantini et al., 2007), to evolve with development and age (Andrews-Hanna et al., 2007; Meunier et al., 2009a) and to be altered by disease state (Greicius et al., 2004; Greicius, 2008; Liu et al., 2008; Baliki et al., 2008; Bassett et al., 2008; Wu et al., 2009; Whitfield-Gabrieli et al., 2009; Buckner et al., 2009) and pharmacological intervention (Kelly et al., 2009).

One analytical approach is provided by graph theory, where the relationships between the signal changes in different brain regions are represented mathematically by a graph (network) comprising a set of vertices (nodes) and inferred connections (edges) between them (Reijneveld et al., 2007; Stam and Reijneveld, 2007; Buckner et al., 2009; Bullmore and Sporns, 2009; Wang et al., 2010a). Networks constructed by retaining the strongest positive correlations as edges have been shown to exhibit a number of interesting—and biologically significant—properties, distinct from randomly or regularly connected graphs. These include “small-world” behavior, in which the connection structure is more highly clustered (cliquish) compared to randomly wired networks with the same degree distribution, despite a similar overall average path length (distance between all pairs of nodes) (Watts and Strogatz, 1998; Bassett and Bullmore, 2006; Bullmore and Sporns, 2009; Wang et al., 2010a; Hayasaka and Laurienti, 2010). This property has also been observed in many other networks from fields such as genetics, protein folding, metabolism, epidemiology and transport (Watts and Strogatz, 1998; Wagner and Fell, 2001; Vendruscolo et al., 2002; Christley and French, 2003; Sienkiewicz and Hołyst, 2005; Zhang and Horvath, 2005; Braun et al., 2006; Almaas, 2007), and this deviation from the behavior of random

\* Corresponding author. Fax: +1 317 433 1071.

E-mail address: [adamschw@indiana.edu](mailto:adamschw@indiana.edu) (A.J. Schwarz).

or regular graphs has led to the term “complex network” for such real-world networks. Another property observed in functional connectivity networks is the presence of relatively few, excessively highly-connected, ‘hub,’ nodes and many more weakly-connected nodes. In particular, a linear dependence (up to a high-degree cut-off) in the histogram of node degree (the number of edges connected to each node) revealed when the distribution is plotted on a logarithmic scale has suggested “scale-free” behavior described by a truncated power law. Finally, networks of functional connectivity have also been shown to be modular, with the overall network able to be segregated into tightly interconnected groups of nodes (He et al., 2009; Schwarz et al., 2009; Meunier et al., 2009b; Ferrarini et al., 2009; van den Heuvel et al., 2009a; Valencia et al., 2009; Shen et al., 2010).

However, the above network construction approach corresponds to selecting some fraction of the right (positive-most) tail of the correlation histogram; to date, the left (negative-most) tail of the histogram, and the interpretation of negative edges within a complex network representation of functional connectivity, has largely been ignored. The network characteristics of the negative-most edges are relevant when deciding how to handle negative correlations within a graph theoretic framework. For example, does it make sense to derive networks from the magnitude of the correlation coefficient  $|r_{ij}|$ , treating correlations and anti-correlations of the same magnitude equally? Does negative valence *per se* matter, i.e., do anti-correlations evoke different graph-theoretic properties than positive edges toward the left tail of the histogram?

An important underlying variable to these questions is the choice of data preprocessing steps, in particular the deconvolution from the grey matter time courses of potential confounding signals prior to computation of the correlation matrix. How does this choice affect the resulting network properties? Some authors appear to have removed no potentially confounding signals (Van den Heuvel et al., 2008; Nakamura et al., 2009; Wang et al., 2010b), some have regressed out head movement time courses (Achard and Bullmore, 2007; Liu et al., 2008; Mumford et al., 2010), some have removed head motion signals along with a global, whole brain average signal (Wang et al., 2009) and several have removed white matter and cerebral spinal fluid (CSF) time courses along with motion traces and the global signal (He et al., 2009; Shehzad et al., 2009; Hayasaka and Laurienti, 2010). Global signal correction in functional connectivity generally is currently the subject of some debate (Vincent et al., 2006; Birn et al., 2006; Chang and Glover, 2010; Murphy et al., 2009; Fox et al., 2009; Schölvinck et al., 2010). A motivation for removing it from the data is to remove non-neural confounds, such as respiration-induced fluctuations, yet this operation can also induce anti-correlations even when none are present in the original data. However, the effects of different confound signal removal strategies on graph theoretic properties of functional connectivity networks have not to our knowledge been addressed.

In binary networks, information contained in the numeric values of sub-threshold inter-node correlations is suppressed (edge values set to 0), and that in supra-threshold correlations is compressed (edge values set to 1). Retaining the supra-threshold edge weights (Nakamura et al., 2009; Wang et al., 2010b) alleviates the latter effect but not the former—small differences in correlation strength, or in the chosen threshold, can result in edges being present or absent in the resulting network. In both approaches, there is an inherent tension between the use of more stringent thresholds, maximizing the contributions from the strongest correlations and emphasizing the network characteristics exhibited more strongly in the extreme (positive) tail of the histogram (Eguiluz et al., 2005; Van den Heuvel et al., 2008), and less restrictive thresholds, minimizing effects due to networks becoming excessively disconnected. In practice, most studies of binary networks have therefore verified results over a range of such thresholds (Achard and Bullmore, 2007; Van den Heuvel et al., 2008; Nakamura et al., 2009; Hayasaka and Laurienti, 2010).

An alternative approach to binarization is to retain all edges, replacing the thresholding operation with a continuous mapping of correlation values  $r$  into edge weights  $w$ . Both linear (Lohmann et al., 2010) and non-linear (Zhang and Horvath, 2005) mappings may be employed. In the latter case, Zhang and Horvath (2005) proposed adjacency functions of a power law form  $w \sim r^\beta$  that emphasized the strongest similarity measures (right tail of the similarity measure histogram) in the context of gene co-expression networks. This was termed ‘soft thresholding,’ in contrast to the traditional ‘hard thresholding’ approaches described above. These mappings have also recently been evaluated in a study of the modular organization of the brain from functional connectivity data (Mumford et al., 2010). Adjacency functions of this form can be designed to map a finite range of similarity measures (e.g.,  $[-1, 1]$  in the case of linear correlations) to a weight  $w_{ij} \in [0, 1]$ , yielding unsigned complete, weighted networks that generalize the adjacency matrix of binary graphs ( $a_{ij} \in \{0, 1\}$ ) whilst retaining the same bounded range. Variants on this include working from the absolute value of a signed correlation value (Zhang and Horvath, 2005), or retaining the valence of edge weights (mapping  $r_{ij} \in [-1, 1]$  to  $w_{ij} \in [-1, 1]$ ). However, this choice should be informed by the network properties as a function of edge strength, in particular those associated with the left tail of the correlation histogram.

In the present study, we examine the graph theoretic properties of networks constructed from the negative-most similarity measures (i.e., the left tail of the correlation histogram), how this is influenced by different strategies for confound signal removal, and consider the within-subject reproducibility of network parameters. Both of these are relevant to the choice of a continuous adjacency function, informing how the similarity measures might best be weighted. Finally, we examine the characteristics and reproducibility of complete, weighted networks of functional connectivity in healthy subjects constructed using continuous adjacency functions.

## Methods

### Resting state fMRI time series data

The present study used the New York University reliability data set downloaded from [www.nitrc.org](http://www.nitrc.org) (M.P. Milham and F.X. Castellanos). This set comprises resting state data originally acquired at 3 T from  $N = 25$  healthy subjects (10 male, 15 female, ages 22–49). A task-free (“resting state”) echo-planar imaging (EPI) time series was acquired three times from each subject—the second and third scans were acquired 45 min apart within the same scanning session, 5–16 months after the first session. Each time series comprised 197 volumes of 39 axial slices with  $T_R = 2$  s. The first two volumes of each were removed for signal intensity equilibration, yielding 6 min 30 s time series. Further acquisition details are provided in (Shehzad et al., 2009).

Each EPI time series was spatially preprocessed as follows, using FMRIB's Software Library (FSL) tools. (1) Motion correction of EPI time series (FSL/McFLIRT); (2) Brain extraction of each EPI time series (FSL/bet2); (3) Affine spatial normalization of the mean image of each time series directly to the SPM EPI template (FSL/FLIRT, 12 degrees of freedom), with registration parameters then applied to time series and the individual brain mask. Finally, (4) a group brain mask was computed as the exclusive-and of all individual (normalized) brain masks and the template intracranial mask.

### Preparation of time courses for network computation

One aim of this study was to determine the impact of different confound signal removal strategies on the resulting network

characteristics. Four different confound signal removal approaches were applied to the preprocessed data:

- (1) No confound signal removal (“none”). In this case, the time series were simply band-pass filtered ( $0.01 < f < 0.1$  Hz).
- (2) White matter and cerebral spinal fluid (CSF) time courses removed, prior to band-pass filtering as per (1) (“WMCSF”). Individual subject signals from deep white matter and ventricular regions were calculated using masks based on the FSL tissue class distribution maps in order to minimize contributions from other tissues. The white matter map was thresholded at 230/255 (~90%) and the CSF map at 191/255 (~75%). Both thresholds were chosen so as to provide conservative, focal masks encompassing only voxels deep within the respective tissue classes and with minimal contamination from other tissues. The CSF mask included third and fourth ventricles.
- (3) White matter, CSF and head motion traces removed, prior to band-pass filtering as per (1) (“WMCSF + mot”). In addition to the white matter and CSF signals as per (2), the six head motion time signals for each subject were also removed.
- (4) Global signal correction (“global”), prior to band-pass filtering as per (1). The whole brain average signal was removed from each subject. Although several authors have deconvolved other confound signals in addition to the global brain mean, the global signal removal dominates the effects on the correlation matrix histogram (cf. (Vincent et al., 2006), Fig. 1).

For each of (1)–(4) the respective potential confound signals were deconvolved from that in each voxel within a gray matter (GM) mask, created by thresholding the FSL gray matter distribution map at 102/255 (~40%). This threshold was selected to retain GM voxels in superior parietal and somatosensory regions that were excluded at higher thresholds (e.g., 50%).

For reasons of computational tractability, VOI scale networks were employed to assess the effects of negative edges and different adjacency functions. Each image time series was parcellated into  $N_{\text{VOI}} = 90$  VOI time courses using the cortical and sub-cortical regions within the automated anatomical labeling (AAL) template (Tzourio-Mazoyer et al., 2002). The mean time course of the voxels within each atlas region was extracted for subsequent network construction.

#### Computation and quantification of networks

Following the preprocessing steps outlined above, correlation matrices  $\{r_{ij}\}$  ( $1 \leq i, j \leq N_{\text{node}}\}$  were calculated as the zero-lag Pearson linear correlation coefficient between all pairs of time courses, where  $N_{\text{node}} = N_{\text{VOI}}$ .

#### Binary networks

Conventional, right-tail binary networks were calculated by retaining correlation values above a given cut-off threshold  $r_c$  and setting their value to unity:

$$a_{ij} = \begin{cases} 1, & r_{ij} \geq r_c, \\ 0, & r_{ij} < r_c. \end{cases} \quad (1)$$

This transforms the correlation matrix into a binary adjacency matrix  $a_{ij}$ , with the non-zero values indicating the edges retained in the network. In an analogous fashion, left-tail binary networks were calculated by retaining correlation values below a cut-off threshold:

$$a_{ij} = \begin{cases} 1, & r_{ij} \leq r_c, \\ 0, & r_{ij} > r_c. \end{cases} \quad (2)$$

There are two approaches to threshold selection in binary networks—the binarization threshold  $r_c$  is typically either set to a fixed value  $-1 < r_c < 1$  and applied to all networks, or calculated for each network such that a consistent average node degree or fraction of the strongest cells in the correlation matrix is retained in each. The former strategy results in “equi-threshold” networks, in which the numeric value of the original similarity measure is consistently mapped to the presence or absence of a link in the binary network (Van den Heuvel et al., 2008; van den Heuvel et al., 2009b; Hayasaka and Laurienti, 2010). In the latter case, “equi-sparsity” networks are computed by calculating network-specific values of  $r_c$ , resulting in networks of the same size with the same fraction of the maximum possible number of connections retained for each. This fraction is referred to as the ‘cost’ (reflecting a ‘wiring cost’ of the network) or ‘sparsity’ (Achard and Bullmore, 2007; Van den Heuvel et al., 2008; Wang et al., 2010b; Hayasaka and Laurienti, 2010). In the present study, we evaluated both equi-sparsity and equi-threshold approaches for both right-tail and left-tail networks.

A range of sparsity values {5%, 10%, 20%, 30%} within the small-world regime (Achard and Bullmore, 2007) were evaluated. Fixed thresholds were determined as the mean threshold, across subjects, corresponding to each of the above sparsity values. For equi-threshold networks, we computed the mean  $r_c$  from the equi-sparsity 10% cohort of networks,  $\bar{r}_c^{(10\%)}$ , and then varied this in steps of 0.1 to generate a range of thresholds as  $\{\bar{r}_c^{(10\%)} + 0.1, \bar{r}_c^{(10\%)} - 0.1, \bar{r}_c^{(10\%)} - 0.2\}$  for right-tail networks and  $\{\bar{r}_c^{(10\%)} - 0.1, \bar{r}_c^{(10\%)}, \bar{r}_c^{(10\%)} + 0.1, \bar{r}_c^{(10\%)} + 0.2\}$  for left-tail networks. For right-tail networks, following WMCSF + mot preprocessing,  $\bar{r}_c^{(10\%)}$  and hence equi-threshold networks were created at thresholds  $r_c \in \{0.81, 0.71, 0.61, 0.51\}$ ; following global signal removal,  $\bar{r}_c^{(10\%)}$  and hence equi-threshold networks were created at

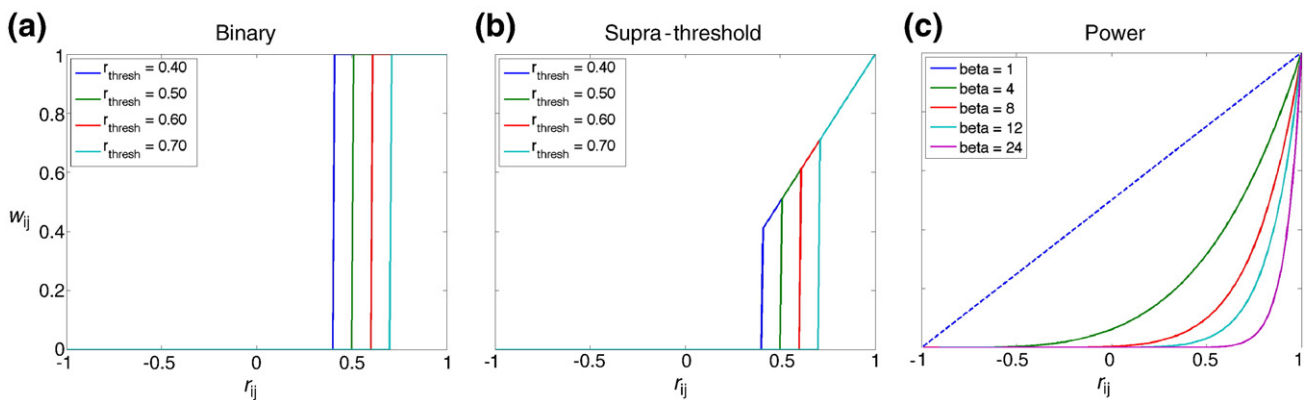


**Fig. 1.** “Hard-thresholding” (a,b) and “soft-thresholding” (c) adjacency functions. Each maps an inter-node correlation coefficient  $r_{ij} \in [-1, 1]$  to a non-negative edge weight  $w_{ij} \in [0, 1]$ . (a) Conventional binary thresholding; edges with correlation strengths above a defined threshold value are assigned the value of unity, those below the threshold are assigned the value 0. (b) Supra-threshold weighting; edges with correlation strengths above a defined threshold retain their value  $w_{ij} = r_{ij}$ , whereas those below the threshold are assigned the value 0. (c) Power adjacency function  $w_{ij} = ((r_{ij} + 1)/2)^\beta$ . (See text for additional details.)

thresholds  $r_c \in \{0.55, 0.45, 0.35, 0.25\}$ . For left-tail networks, following WMCSF + mot preprocessing,  $\bar{r}_c^{(10\%)} = 0.16$  and hence equi-threshold networks were created at thresholds  $r_c \in \{0.06, 0.16, 0.26, 0.36\}$ ; following global signal removal,  $\bar{r}_c^{(10\%)} = -0.40$  and hence equi-threshold networks were created at thresholds  $r_c \in \{-0.50, -0.40, -0.30, -0.20\}$ . For comparison,  $r$  values corresponding to  $p = 0.05$  are 0.14 (uncorrected) and 0.31 (family-wise error corrected).

We also examined the properties of networks constructed from intermediate correlation values in order to understand the topological properties of edges derived from intermediate correlation strengths and the transition between network behavior in the left and right tails of the histogram. Each subject's correlation histogram was divided into deciles and, for each decile, networks of 10% sparsity were generated from the connections with correlation values only within the range corresponding to that decile. The first decile thus corresponded to the left-tail network of 10% sparsity and the tenth to the right-tail network of 10% sparsity. Intermediate decile networks excluded contributions from correlations stronger and weaker than those within the specific range of that decile. Working with equi-sparse networks for this purpose allowed for the different profiles and offsets in the individual subject histograms and avoided issues with networks becoming overly dense or overly sparse (disconnected) at the extremes of the distribution if fixed thresholds were used. To reflect the histogram shifts due to the different preprocessing strategies, the graph parameters were plotted against the average value of  $r$  within each decile, across subjects.

We evaluated the binary networks using the graph theory parameters summarized in Table 1, calculated using the Brain Connectivity Toolbox (<http://www.brain-connectivity-toolbox.net>) (Rubinov and Sporns, 2010) within the Matlab scientific computing environment (<http://www.mathworks.com>). Random comparator networks for formal comparison with *in vivo* networks were generated by randomly rewiring the network connections such that the original degree sequence is preserved (Maslov and Sneppen, 2002) and were used in the computation of  $\gamma$  and  $\sigma_{sw}$ . Random networks of the same size (numbers of nodes and edges) as the *in vivo* networks but not constrained to have the same degree sequence were also calculated and their properties shown for qualitative comparison.

### Weighted networks

The binarization step above (Eq. (1), Fig. 1(a)) can be considered one instance of a more general class of adjacency functions  $w_{ij} = f(r_{ij})$  that map the inter-node correlation coefficient  $r_{ij} \in [-1, 1]$  to a non-negative edge weight  $w_{ij} \in [0, 1]$  ( $1 \leq i, j \leq N_{\text{node}}$ ). Weighted networks

can be defined by retaining the numeric values of the supra-threshold cells in the correlation matrix (Fig. 1(b)):

$$w_{ij} = \begin{cases} r_{ij}, & r_{ij} \geq r_c, \\ 0, & r_{ij} < r_c. \end{cases} \quad (3)$$

However, both Eqs. (1) and (3) represent 'hard thresholding' approaches—edges weaker than the threshold are eliminated.

We thus also evaluated a family of 'soft-thresholding' adjacency functions (Zhang and Horvath, 2005) defined by a power adjacency function (Fig. 1(c)):

$$w_{ij} = \left( \frac{r_{ij} + 1}{2} \right)^\beta. \quad (4)$$

Here,  $w_{ij} = f(r_{ij}, \beta)$  describes a continuous, non-linear mapping of correlation coefficients (or related similarity measures in the range  $[-1, 1]$ ) to edge weights  $w_{ij} \in [0, 1]$  and results in unsigned, complete, weighted networks in which all edges are retained. When  $\beta = 1$ , this corresponds to a linear mapping and simply compresses the original correlation values into the non-negative range. In this linear limit, signed transformations are also possible, retaining edge valence and assigning edge weights as  $w_{ij} = r_{ij}$ . In this study, we concentrated on an evaluation of unsigned networks, in order to assess their properties using parameters analogous to those established for hard-thresholded networks. Many graph theoretic measures have been defined only for hard thresholded networks (Rubinov and Sporns, 2010). We thus characterized soft-thresholded networks in terms of the node strength

$$s_i = \sum_j w_{ij}, \quad (5)$$

a generalization of node degree  $k_i = \sum_j a_{ij}$  in binary networks, and the node clustering coefficient  $c_i$ , generalized for continuously-valued edge weights  $0 < w_{ij} < 1$  (Zhang and Horvath, 2005):

$$c_i = \frac{\sum_{u \neq i} \sum_{v \neq i, v \neq u} w_{iu} w_{uv} w_{vi}}{(\sum_{u \neq i} w_{iu})^2 - \sum_{u \neq i} w_{iu}^2}. \quad (6)$$

A random comparator network with an equivalent strength distribution was computed for each soft thresholded network by generating a similarity matrix whose off-diagonal entries were randomly generated under a Gaussian distribution of mean and variance equivalent to the *in vivo* similarity matrix. (Any values

**Table 1**  
Graph theoretic parameters examined for binary networks.

Local (nodewise) parameter	Global (network average) parameter	Definition
$k_i$	$K$	Node degree, a count of the number of links attached to the node. Range $[0, N_{\text{node}}]$ .
$c_i$	$C$	Clustering coefficient, a measure of cliquishness—how many of a node's neighbors are also connected amongst themselves. Range $[0, 1]$ .
–	$A$	Assortativity, a correlation between the degrees of nodes on the opposite ends of the edges in the network. Positive values indicate that nodes tend to attach to others of a similar degree. Range $[-1, 1]$ .
–	$L$	Characteristic path length, the average distance between all pairs of nodes.
$E_{l,i}$	$E_{loc}$	Local efficiency. Range $[0, 1]$ .
$E_{g,i}$	$E_g$	Global efficiency. Range $[0, 1]$ .
–	$Q$	Modularity. A measure of the degree to which the network can be segregated into tightly-interconnected 'modules'. Range $[0, 1]$ .
–	$G$	Giant component. The largest fraction of the network for which all nodes are connected to all other nodes. Range $[0, 1]$ .
–	$\gamma$	Ratio of the mean clustering coefficient to the mean clustering coefficient in a randomly wired network with the same degree distribution ( $C/C_{\text{ran}}$ ). High clustering signaled by values $\gamma \gg 1$ is indicative of "small-world" behavior.
–	$\sigma_{sw}$	Ratio of $\gamma$ to $\lambda = L/L_{\text{ran}}$ , where $L_{\text{ran}}$ is the characteristic path length of a randomly wired network with the same degree distribution.



outside the range  $[-1, 1]$  were recomputed under the distribution until all values were within this range.) The same adjacency function transformation used in the generation of the *in vivo* network was then applied to this matrix.

#### Data visualization and statistical measures

Where appropriate, quantities are displayed as boxplots showing the median, 25th–75th quartile range and full range across samples or parameters, with outliers displayed as individual ‘+’ markers.

Networks were visualized as intensity plots of edge weight or edge incidence, cumulative across subjects, with nodes ordered to emphasize block-diagonal modular structure. Binarized networks were also visualized using ordered edge incidence matrices to emphasize modular structure and ipsi-contralateral connections (when present) and using hierarchical edge bundles (Holten, 2006; McGonigle et al., 2011). The hierarchy used here is based on that proposed in Tzourio-Mazoyer et al. (2002) and as such those functional regions in close spatial proximity to one another are more likely to appear close in a ring representation (the indentation level showing the level of hierarchy). Edges are modeled as B-splines, with those following a similar path to one another within the hierarchy being grouped together for relevant subsections of their paths. Those bundles containing a greater number of edges are rendered as being darker in color.

Comparisons of single parameters between groups, sessions or preprocessing conditions were performed using Student's t-test, paired or unpaired as appropriate. Reproducibility of the correlation histograms and graph theoretic network parameters was quantified by the intra-class correlation coefficient (ICC) (Shrout and Fleiss, 1979; McGraw and Wong, 1996). Specifically, we employed

$$\text{ICC}(1, 1) = \frac{\text{BMS} - \text{WMS}}{\text{BMS} + (k - 1)\text{WMS}}, \quad (7)$$

in the notation of Shrout and Fleiss (1979) (equivalent to ICC(1) in the notation of McGraw and Wong (1996)). Here, BMS is the between-subject least squares error, WMS is the within-subject least squares error and  $k$  is the number of sessions. This variant of the ICC measures the absolute agreement between the numeric endpoints at the two or three different scanning sessions and is relevant to a one-way analysis of variance analysis of an intervention study on these measures (as a simple example, a randomized two-scan placebo/drug study analyzed using a two-sample t-test). Other ICC variants include other individual sources of error—for example, scan order—explicitly and may be appropriate to more sophisticated analyses planned for intervention or case-control studies. For the purposes of the present work, we were most interested in comparative reproducibility of results obtained using variants of the analysis methodology on the same data. The main conclusions reported here for ICC(1,1) held if other ICC variants were used.

## Results

#### Correlation strength distributions

In the absence of any confound signal removal, the  $r_{ij}$  distributions were substantially right-shifted, with most inter-node correlation values positive and fewer than 10% negative (Fig. 2). There was some variability across subjects in the histograms, with several showing distributions more strongly skewed toward  $r_{ij} = 1$ . Deconvolution of individual-subject white matter and CSF signals, both with and without the inclusion of motion regressors, resulted in slight leftward shifts in the distributions and small increases in the number of negatively-valued coefficients. In contrast, removal of the global average brain signal from each subject resulted (by construction) in

histograms centered close to zero with substantially reduced variability across subjects.

Despite the between-subject variability in  $r_{ij}$  distributions in the absence of global signal correction, we found these to be reasonably reproducible within subjects. The mean histogram values  $r$  demonstrated ICC values in the range 0.41–0.64, depending on preprocessing strategy and which scanning sessions were compared (Table 2). As expected, reproducibility between sessions 2 and 3 (45 min apart) was higher than that between sessions 1 and 2 (5–16 months apart). Moreover, despite the relatively subtle effect of the confound signal removal on the histograms, there was a consistent trend to higher ICCs with the removal of more confounding variations (WMCSF + mot > WMCSF > none) with values 0.50–0.64 following deconvolution of white matter, CSF and head motion signals. (Globally-corrected histograms were not analyzed in this respect as the global signal correction yields, by construction, histogram means  $\sim 0 \pm$  residual error.)

#### Intermediate network parameter values and left-tail networks

Networks constructed from the positive-most tails of the  $r_{ij}$  histogram exhibited elevated clustering coefficients ( $C \sim 0.5$ ) relative to randomly rewired comparator networks ( $\gamma \sim 2.5 - 3.5$ ), indicative of “small world” behavior (Fig. 3, Table 3). These right-tail networks were also assortative ( $A \sim 0.35$ ) and modular ( $Q \sim 0.5$ ), with strong inter-hemispheric links between corresponding ipsi- and contralateral brain regions (Figs. 4(a,d)). These properties were maintained for all confound signal removal strategies, with slightly higher values of  $C$ ,  $\gamma$  and  $Q$  following global signal removal.

The properties associated with the positive tail dropped off rapidly in networks constructed from intermediate correlation values, with network parameters converging to values similar to those of random networks constrained only to have the same number of nodes and edges (Fig. 3). Networks created from the negative-most tail of the histograms had characteristics distinct from those observed in positive-tail networks, and these were qualitatively different following global signal removal compared with the other three confound signal preprocessing strategies (Fig. 3, Table 3). The largest connected component in the networks comprised the complete network at intermediate correlation values and represented  $\geq 90\%$  of the network on average at both right-tail and left-tail extremes (see Supplemental Data).

In the absence of global signal removal,  $r_{ij}$  values in the left tail were around zero, reflecting weak correlations. Left-tail network parameters remained distinct from right-tail values, with the clustering coefficient  $C \sim 0.1$ ,  $\gamma \sim 0.35$ , modularity  $Q \sim 0.25$  and assortativity  $A \sim 0.5$ .

Following global signal removal, these characteristics were substantially altered. The clustering coefficient  $C$  (and hence  $\gamma$  and  $\sigma_{sw}$ ) was suppressed to near zero, whereas assortativity  $A \sim 0$  and modularity  $Q \sim 0.3$  had values higher than without global signal removal and similar to those obtained from random networks. Local efficiency  $E_{\ell}$  followed a similar pattern to  $C$ , whereas the global efficiency,  $E_g$ , maintained values  $\sim 0.4 - 0.5$  for both right- and left-tail networks, with and without global signal removal (Table 3).

Overall, negative-tail networks showed a weaker and less consistent structure than positive-tail networks. This was observed over the range of sparsities and thresholds tested, and is illustrated in Fig. 4 for equi-sparse networks constructed at a cost of 10%. The nodes in Figs. 4(d,g) are ordered as per Figs. 4(c,f) but did not reveal the characteristic block-diagonal structure of modular networks when independently ordered based on the best modular decomposition (see Supplemental Data); this is consistent with the low modularity values in left-tail networks (Fig. 3). Edges linking the supramarginal gyrus with the medial orbital cortex and the posterior cingulate gyrus were observed consistently in left-tail networks for

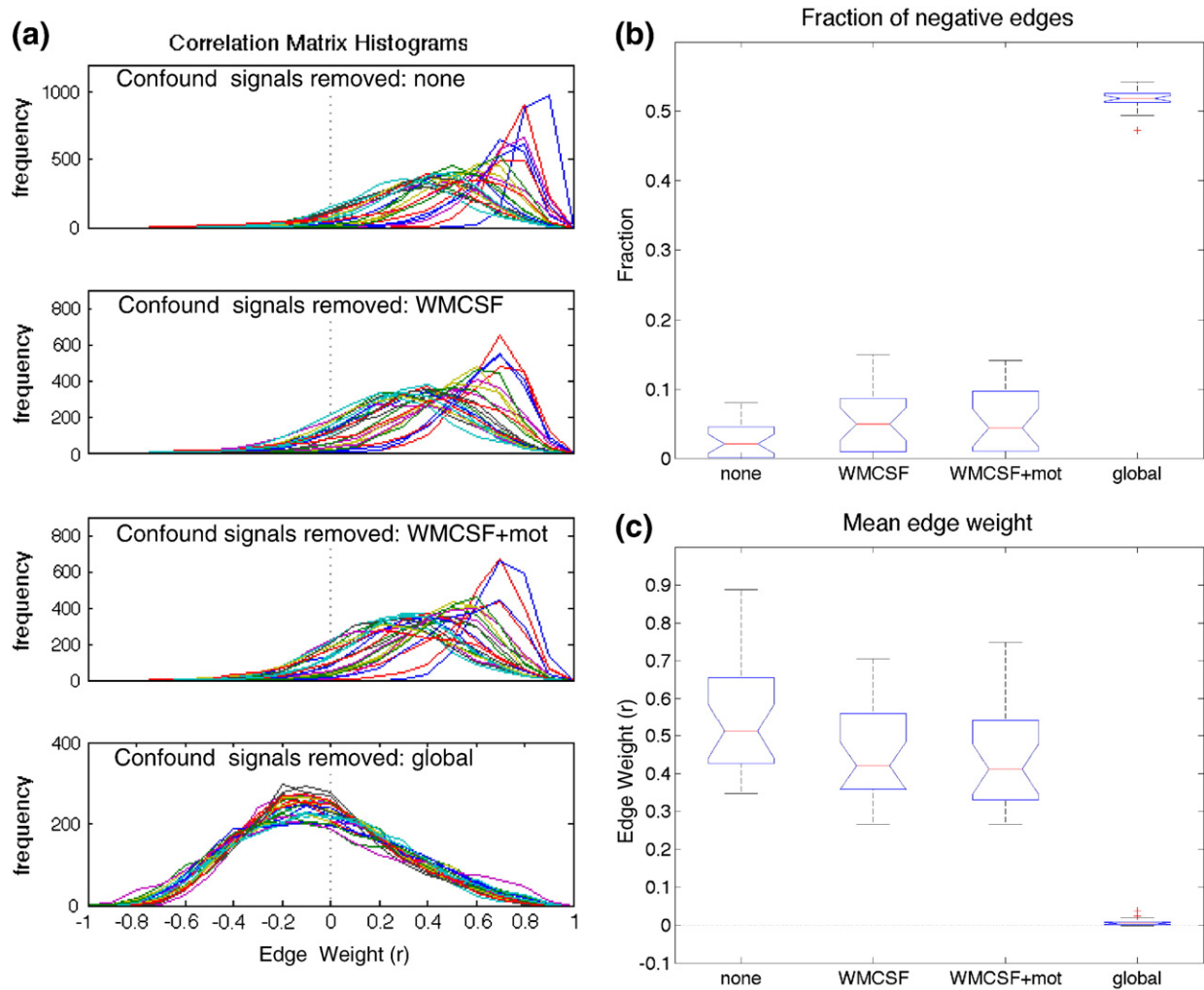


**Fig. 2.** Effect of confound signal removal preprocessing strategy on correlation matrix histogram and edges of negative valence. (a) Individual subject histograms of correlation matrices ( $r_{ij}$ ). From top to bottom: no confound signal removal; white matter and CSF signal removal; white matter, CSF and motion regressor ( $\times 6$ ) removal; global signal removal. Different colored lines indicate different subjects (session 1). (b) Fraction of arithmetically negative correlation values. (c) Histogram centroids (mean inter-node correlation coefficients). Boxplots represent median, 25th and 75th quartiles and range across subjects.

both WMCSF + mot and global signal removal (Table 4). In the absence of global signal correction these connections had the consistently lowest correlation coefficients but these were not always of negative valence.

Without global signal removal, taking the magnitude of the correlation matrices prior to binarization had little effect on networks constructed from the tail of the distribution for the present data, since it folded weak negative correlations to weak, sub-threshold positive ones. In the case of global signal correction, however, the negative tail folded across to the positive tail and network properties resulting from absolute value correlation matrices were significantly altered (Fig. 4).

**Table 2**  
Intra-class correlation coefficients of correlation matrix histogram centroids.

ICC(1,1)		Confound signal removal strategy		
		None	WMCSF	WMCSF + mot
Sessions	1–2	0.41	0.44	0.50
	2–3	0.49	0.59	0.64
	1–2–3	0.42	0.48	0.51

#### Reproducibility of binary network properties

Within-subject reproducibility of positive-tail binary networks was assessed by the intra-class correlation coefficient across various network parameters. Equi-threshold networks exhibited more robust reproducibility across the three scanning sessions than equi-sparse networks (Fig. 5). This observation was consistent across the different preprocessing schemes, although performance was most robust when white matter, CSF and motion signals, but not the global brain signal, were removed. These findings also held across a range of sparsities and fixed thresholds (see Supplemental Data). Clustering coefficient  $C$  and local efficiency  $E_l$  were the most reproducible parameters, especially in left-tail networks.

#### Soft-thresholded networks

Histograms of edge weight  $w_{ij}$  following soft-thresholding transformations at different values of  $\beta$  are illustrated in Fig. 6 for WMCSF + mot preprocessing. A linear mapping ( $\beta = 1$ ) of  $r_{ij}$  to  $w_{ij}$  yielded edge weight distributions reflecting the original  $r_{ij}$  distribution (Fig. 6 (a), cf. Fig. 2(a)), with most edges having weights  $0.5 \leq w_{ij} \leq 1$ . As  $\beta$  was increased, the edge weight distributions became increasingly skewed toward lower values of  $w_{ij}$  (Figs. 6(b–d)).

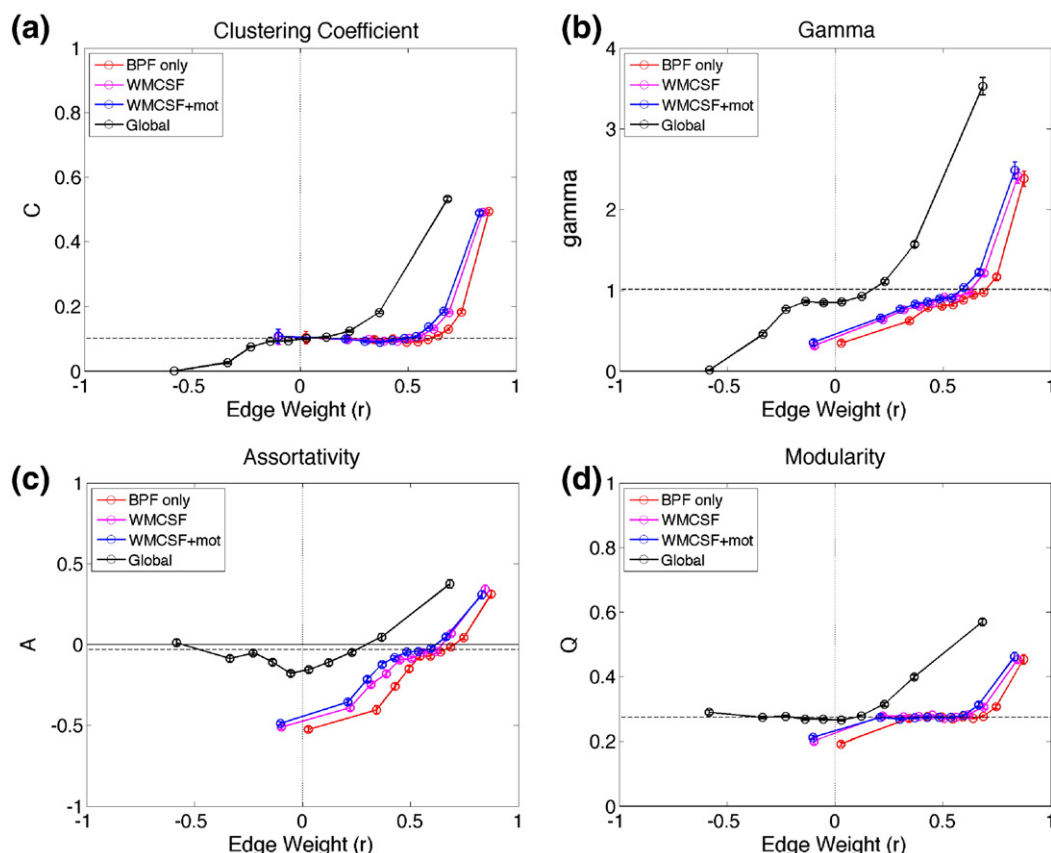


**Fig. 3.** Graph theoretic properties of binary networks constructed from edges in deciles across the full correlation coefficient histograms. Parameter values are plotted against the mean  $r_{ij}$  value across subjects for each decile. Each line represents a different confound signal removal strategy. The dashed horizontal line indicates the value obtained from random networks with the same number of nodes and edges as the *in vivo* networks as a visual comparison. (a) Clustering coefficient ( $C$ ). (b)  $\gamma = C/C_{\text{ran}}$ , the ratio of  $C$  to that obtained from randomly rewired networks, i.e. having the same degree distribution as the *in vivo* data. (c) Assortativity ( $A$ ). (d) Modularity ( $Q$ ).

The resulting histograms of node strength (the weighted generalization of node degree) distribution are shown in Fig. 7(a). Those for the linear mapping (power function,  $\beta = 1$ ) were strongly skewed toward high to maximal ( $s \sim N_{\text{node}}$ ) values. Increasing  $\beta$  resulted in the distributions becoming more left shifted and approaching the power law dependence (up to a high-strength cutoff) observed in hard-thresholded networks based on the positive tails of the correlation distributions. Higher values of  $\beta$  also resulted in networks that were

more strongly clustered than random comparator networks, indicative of increasingly “small-world” behavior with increasing  $\beta$  (Fig. 7(b)).

#### Reproducibility of soft-thresholded networks

Soft-thresholded weighted networks showed robust within-subject reproducibility in node strength  $S$  and clustering coefficient  $C$  across sessions ( $\text{ICC}(1,1) \sim 0.5–0.6$ ) over a range of  $\beta$  values (Fig. 8), very similar to values obtained for binary and supra-threshold networks over a range of hard thresholds. However, the reproducibility decreased for the session 1 to session 2 comparison (5–16 month interval) at  $\beta \geq 12$ .

#### Correspondence between node parameters in soft-thresholded and hard-thresholded networks

Finally, we assessed the extent to which nodewise parameters corresponded between soft- and hard-thresholded (positive tail) networks; that is, whether nodes with high  $s_i$  (or  $c_i$ ) in the former also tended to have high  $k_i$  (or  $c_i$ ) in the latter. This correspondence depended on the value  $r_c$  of the hard threshold and on the parameter  $\beta$  of the soft-threshold adjacency function; in general, higher values of  $r_c$  yielded optimal correspondence with higher values of  $\beta$ . Correspondence of  $s_i$  was stronger than that for  $c_i$  across a range of thresholds and  $\beta$  values. Fig. 9 illustrates this correspondence for various values of  $\beta$  and for hard thresholded networks constructed using  $r_c = 0.71$  (the mean threshold for binary networks of 10% sparsity). In this example, the strongest correspondence with both binary and supra-threshold weighted networks was observed with  $\beta \sim 12–24$  for both  $s_i$  and  $c_i$  (Figs. 9(a,b)). The dynamic range in both

**Table 3**  
Global parameter values from positive-tail and negative-tail networks (at 10% sparsity).

Mean (range) of parameter values		Pos-tail networks		Neg-tail networks	
Parameter	Preprocessing	Mean	Range	Mean	Range
$C$	WMCSF + mot	0.49	(0.42–0.56)	0.11	(0.01–0.49)
	Global	0.53	(0.46–0.61)	0.00	(0.00–0.00)
$L$	WMCSF + mot	2.12	(2.02–2.37)	2.15	(2.00–2.54)
	Global	2.04	(2.00–2.17)	2.12	(2.00–2.43)
$A$	WMCSF + mot	0.31	(0.12–0.56)	−0.48	(−0.56–−0.37)
	Global	0.37	(0.13–0.68)	0.01	(−0.24–0.17)
$E_g$	WMCSF + mot	0.44	(0.39–0.52)	0.51	(0.49–0.55)
	Global	0.39	(0.32–0.42)	0.46	(0.44–0.47)
$E_i$	WMCSF + mot	0.62	(0.55–0.69)	0.16	(0.01–0.71)
	Global	0.67	(0.61–0.72)	0.00	(0.00–0.00)
$Q$	WMCSF + mot	0.46	(0.34–0.57)	0.20	(0.14–0.27)
	Global	0.57	(0.48–0.64)	0.29	(0.22–0.36)
$G$	WMCSF + mot	0.94	(0.84–0.99)	0.93	(0.79–1.00)
	Global	0.98	(0.92–1.00)	0.94	(0.82–1.00)
$\sigma_{sw}$	WMCSF + mot	2.55	(1.54–3.94)	0.35	(0.09–0.72)
	Global	3.55	(2.13–4.90)	0.01	(0.00–0.12)
$\gamma$	WMCSF + mot	2.55	(1.54–3.94)	0.35	(0.09–0.72)
	Global	3.55	(2.13–4.90)	0.01	(0.00–0.12)



parameters across nodes was lower in the soft-thresholded networks (Figs. 9(c,d)). Lower thresholds  $r_c$  were associated with lower values of  $\beta$  for optimal correspondence (e.g.,  $\beta \sim 8 - 12$  at  $r_c = 0.61$ ).

Soft-thresholded networks also retained a modular structure similar to that of the hard-thresholded versions (Fig. 10). This structure was present following the linear transformation ( $\beta = 1$ ),

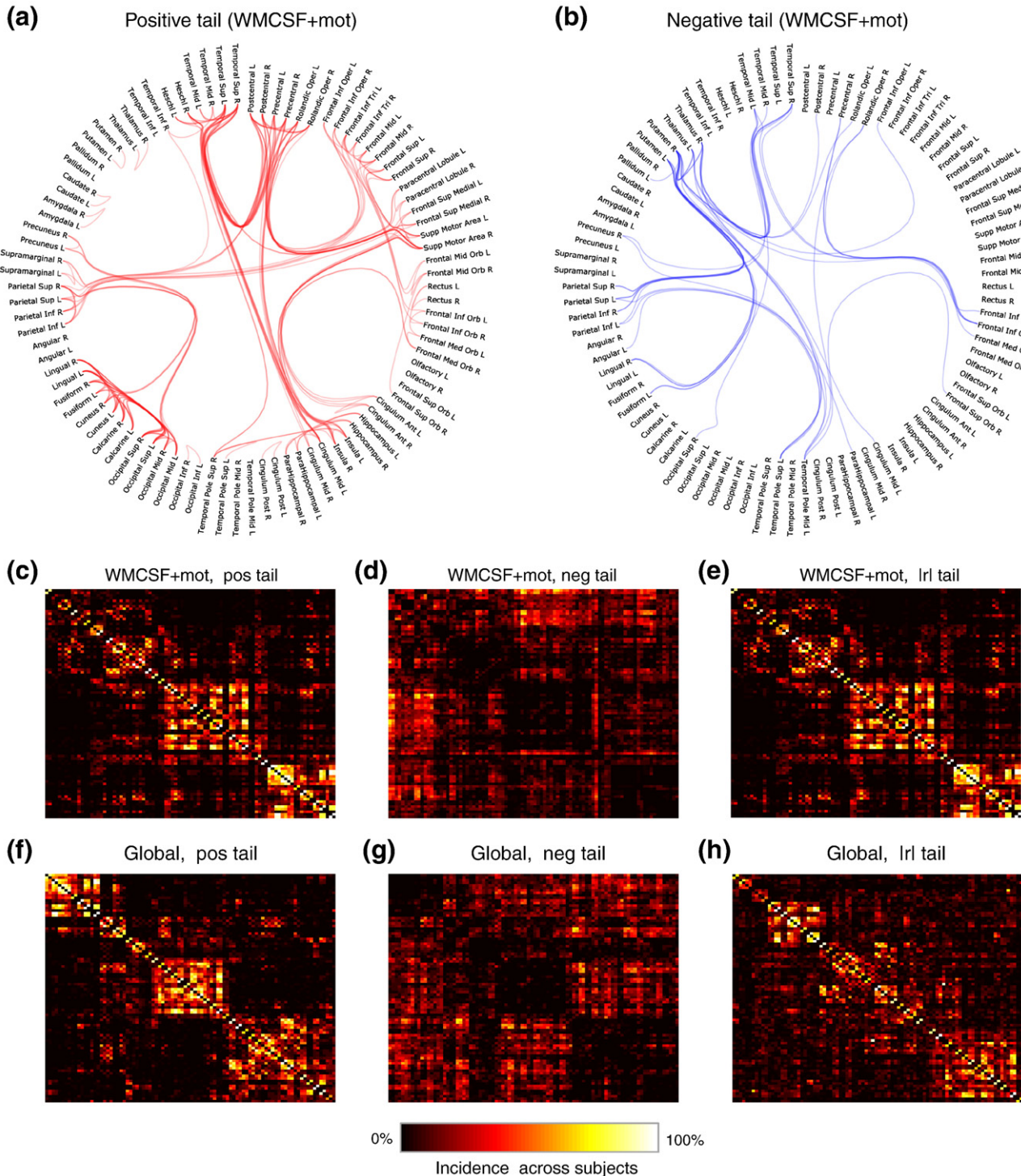


**Fig. 4.** Right and left tail networks. (a,b) Hierarchical edge bundles illustrate the lack of local connections in left tail networks, in contrast to the combination of both short-range and long-range connections in right tail networks. (c–h) Effect of constructing networks from the magnitude of the correlation matrix as a function of preprocessing method. Networks represent the average across subjects, with the edges most consistently present appearing in hotter colors. The node order was determined for the right tail networks to highlight the modular structure and the same order applied to the left tail and absolute value networks, for each preprocessing scenario. Hence, the node order is the same in (c,d,e) and in (f,g,h). [Brain regions corresponding to each node are provided in the Supplemental Data.] (i–k) Quantitative effect of constructing networks from the magnitude of the correlation value on global graph theoretic parameters. For WMCSF + mot signal removal, only weak negative correlations were present and effects on the positive tail were minimal (e,i). With global signal removal, the effects were pronounced, with substantial changes to many network parameters ( $***p < 0.001$ ,  $**p < 0.01$ ) (h,j). Small-world properties of the networks, as indicated by  $\gamma$ , were also compromised in the case of global signal removal (k). These diagrams were computed using indicative networks of 10% sparsity. Hierarchical edge bundles depict connections present with  $> 50\%$  incidence across subjects in WMCSF + mot networks.



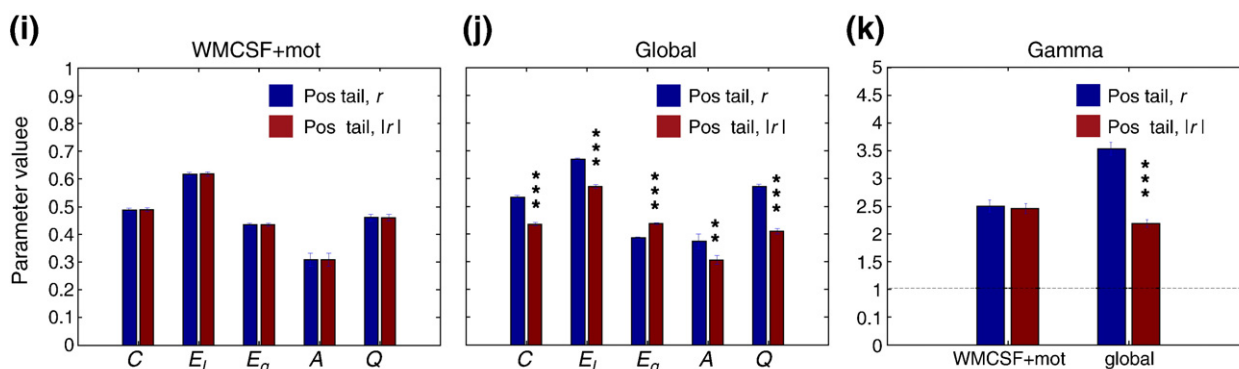


Fig. 4 (continued).

even though the dynamic range of mean weight values across edges was reduced (0.48–0.97 for these data) relative to weights computed using higher values of  $\beta$  (Fig. 10(b), cf. Fig. 6).

## Discussion

### Effect of pre-processing strategy on graph characteristics

An important factor influencing the similarity measures from which the networks are constructed is the choice of data preprocessing steps—in particular the influence of different confound signal removal strategies. The effect of global signal removal in functional connectivity is currently a subject of debate (Fox et al., 2009; Schölvinck et al., 2010). The motivation for this operation is to remove spurious, non-neurogenic contributions to the low frequency signals of interest, arising from changes in respiratory rate for example (Birn et al., 2006), yet it mathematically induces anticorrelations even when none are present in the data (Murphy et al., 2009). However, the influence of different signal removal approaches on graph theoretic properties had not yet, to our knowledge, been systematically studied. Consistent with results from seed region analyses (Vincent et al., 2006; Chang and Glover, 2010; Murphy et al., 2009), we found that deconvolution of white matter, CSF and motion signals left the correlation matrix histograms substantially right-shifted and dominated by positive correlation values, with the left tails comprising weak correlations around zero. This was in contrast to the highly symmetric, zero-centered (by construction) histograms following global signal removal (cf. (Murphy et al. (2009))). This is also consistent with observations from seed region approaches of more focal positive correlations with motor cortex seeds (Vincent et al., 2006) and,

in relation to a posterior cingulate/precuneus seed, more widespread negative correlations (Chang and Glover, 2010) following global signal removal. Our finding that the within-subject reproducibility was optimized with the removal of individual subject white matter, ventricle and head motion time courses accords with the finding of head motion as a substantial component of spurious variance (Jo et al., 2010).

However, the graph theoretic properties of networks created from the correlation histograms are not easily inferred directly from the shifts in these distributions. Examination of networks constructed from the right (positive-most) tail of the histograms revealed properties consistent with many previous reports (Bassett and Bullmore, 2006; Bullmore and Sporns, 2009; Wang et al., 2010a; Hayasaka and Laurienti, 2010), including elevated clustering, local efficiency and modularity compared with random comparator networks, and degree distributions characterized by many low-degree nodes and relatively few high-degree 'hubs'. Interestingly, several of these parameters (in particular  $Q$ ,  $\gamma$ ,  $\sigma_{sw}$ , and to a lesser extent  $C$ ,  $A$  and  $E_1$ ) were slightly increased in value following global signal removal compared with the other confound signal removal strategies. The effect of white matter, CSF and motion time course deconvolution on these properties was subtle, with the parameter profiles slightly left-shifted due to the histogram shift but not otherwise altered (Fig. 3).

In addition to the preprocessing strategies considered here, several methods have been proposed in order to more explicitly account for potential confounding low-frequency effects due to variations in heart and respiration rates (Glover et al., 2000; Birn et al., 2006; Shmueli et al., 2007). Such approaches have been shown to increase the number of anti-correlations between networks defined using seed region

**Table 4**  
Connections most consistently observed in negative tail networks. Normal text denotes edges observed across all four sparsities (costs  $\in \{5\%, 10\%, 20\%, 30\%\}$ ) and thresholds ( $r_c \in \{0.06, 0.16, 0.26, 0.36\}$  for WMCSF + mot,  $r_c \in \{-0.5, -0.4, -0.3, -0.2\}$  for global); italic text denotes edges observed in three of the four sparsities or thresholds.

	Equi-sparse networks	Equi-threshold networks
WMCSF + mot	Frontal Medial Orbital–Supramarginal Gyrus Posterior Cingulate Gyrus–Supramarginal Gyrus Posterior Cingulate Gyrus–Rolandic Operculum Posterior Cingulate Gyrus–Insula	Frontal Medial Orbital–Supramarginal Gyrus Posterior Cingulate Gyrus–Supramarginal Gyrus Posterior Cingulate Gyrus–Rolandic Operculum Posterior Cingulate Gyrus–Insula Supramarginal Gyrus–Mid Temporal Pole Supramarginal Gyrus–Rectus Posterior Cingulate Gyrus–Frontal Inferior Operculum
Global	Frontal Medial Orbital–Supramarginal Gyrus Posterior Cingulate Gyrus–Supramarginal Gyrus Anterior Cingulate Gyrus–Superior Parietal Cortex Frontal Superior Medial Cortex–Superior Parietal Cortex  Anterior Cingulate Gyrus–Superior Occipital Cortex Posterior Cingulate Gyrus–Precentral Gyrus Frontal Superior Medial Cortex–Superior Occipital Cortex	Frontal Medial Orbital–Supramarginal Gyrus Posterior Cingulate Gyrus–Supramarginal Gyrus Anterior Cingulate Gyrus–Superior Parietal Cortex Frontal Superior Medial Cortex–Superior Parietal Cortex Rectus–Supramarginal Gyrus Anterior Cingulate Gyrus–Superior Occipital Cortex Posterior Cingulate Gyrus–Precentral Gyrus Frontal Superior Medial Cortex–Superior Occipital Cortex

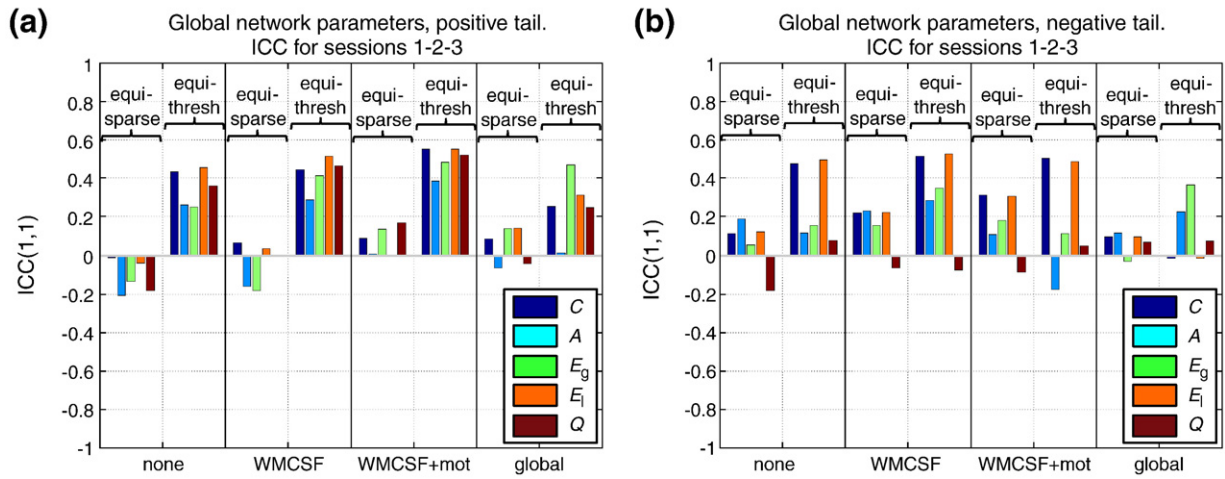


**Fig. 5.** ICC values of global network parameters for positive and negative edge networks with equi-sparse and equi-threshold construction, for the different preprocessing schemes. (a) Positive tail networks. (b) Negative tail networks. ICC values are shown for networks constructed at 10% sparsity and at a fixed threshold corresponding to the mean  $r_c$  of the equi-sparse networks.

approaches in the absence of global signal regression (Chang and Glover, 2009). However, such methods require measurements of respiration and heart rate, which were not available for the data used in the present investigation. Based on Chang and Glover (2009) we might expect the histogram shifts with explicit physiological correction to be intermediate between those found with white matter, CSF and head motion deconvolution and those found with global signal deconvolution in the present study—although the effects of this on resulting graph theoretic parameters and network topology remains to be elucidated.

#### Left-tail networks

In contrast, the properties of networks constructed from the left (negative-most) tails of the correlation histograms were qualitatively different to those of positive tail networks, and these were strongly dependent on whether or not the global signal was removed. In the absence of global signal deconvolution, network parameters resulting from intermediate correlation strengths decreased toward the left tail of the histograms (see Fig. 3). This is consistent with observed

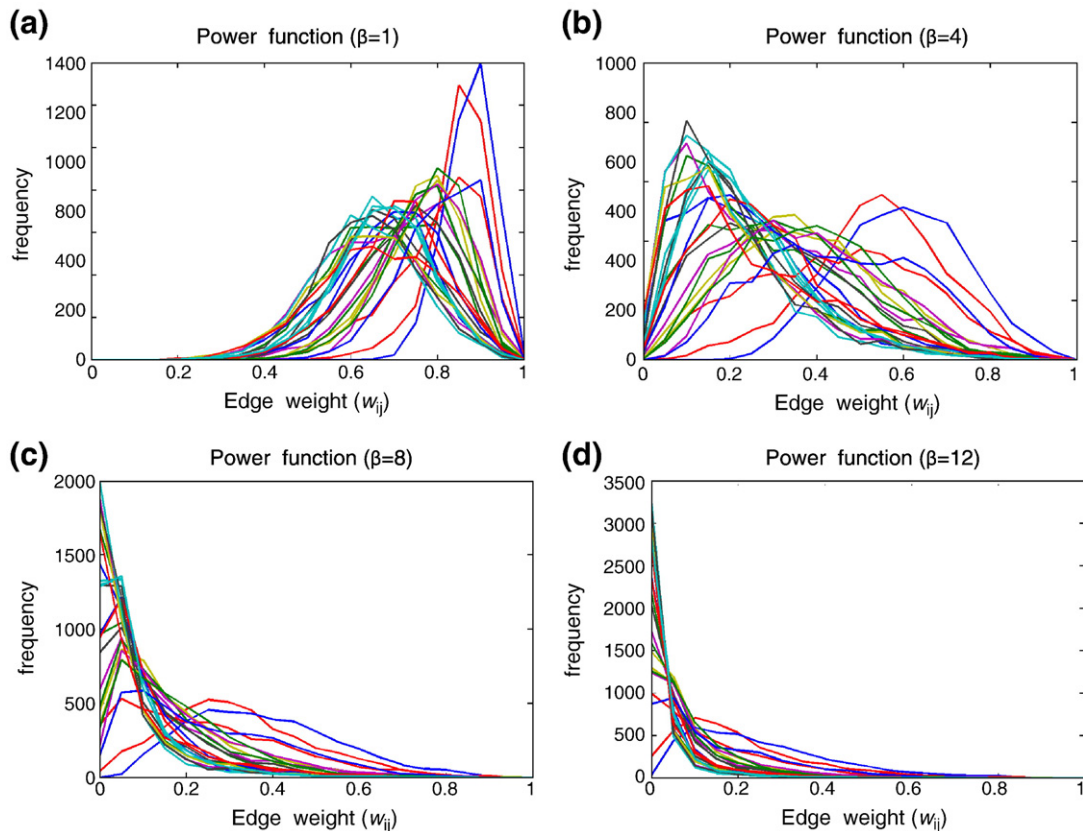


**Fig. 6.** Edge weight distributions of soft-thresholded networks, following WMCSF + mot preprocessing, for different values of the transformation parameter  $\beta$ . Different colored lines indicate different subjects from the first scanning session (cf. Fig. 2(a)).

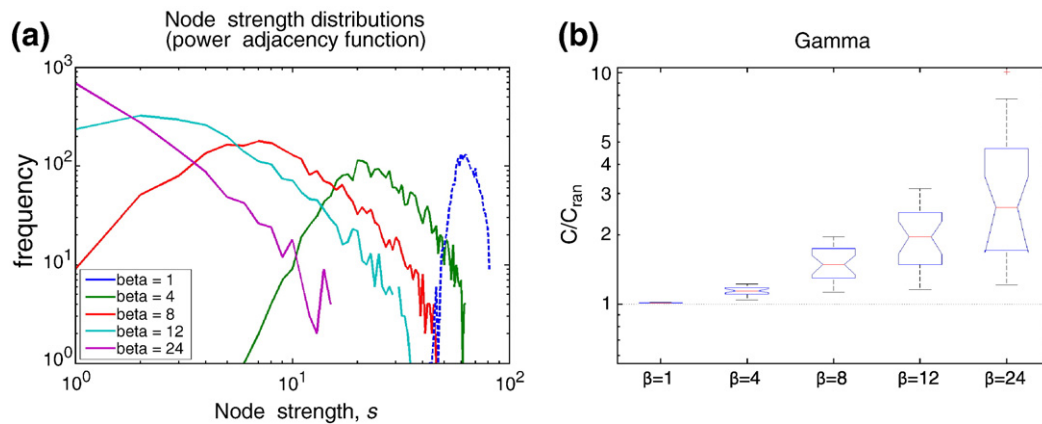


**Fig. 7.** (a) Distributions of node strength ( $s$ ) in soft-thresholded networks using the power adjacency function at various values of  $\beta$ . (b) At sufficiently high values of  $\beta$ , these networks evidence a higher degree of clustering than randomly rewired comparator networks, evidenced by  $\gamma = C/C_{\text{rand}}$ . Boxplots represent median, 25th and 75th quartiles and range.

reductions in these parameters with decreasing  $r_{ij}$  threshold or increasing wiring cost (Eguiluz et al., 2005; Achard and Bullmore, 2007; Van den Heuvel et al., 2008), where edges from the positive-most tail of the histogram are combined with increasing numbers of edges corresponding to intermediate  $r_{ij}$  values. Intermediate weight edges alone thus contributed less cliquish (lower  $C$ ), less “locally efficient” (lower  $E_L$ ) and less modular (lower  $Q$ ) behavior. The assortativity of the intermediate networks converged to near zero toward the middle of the correlation range, but decreased toward the left tail of the histogram reflecting disassortative network behavior indicating that the negative-most edges tend to connect nodes of different degree.

In the absence of global signal removal, the left tails of the histograms had values around zero; the topology observed in left tail networks is thus associated with very weak correlations that may not be biologically meaningful. The leftmost extremities of the correlation histograms in some subjects remained positive but did not substantially alter the network behavior; rather, the left-tail properties for most parameters continued trends apparent at intermediate correlation values. Following global signal removal, the clustering coefficient, assortativity and  $\gamma$  were close to zero and modularity had a value similar to random networks, despite similar overall path lengths. This again indicates little in the way of interesting structure. Although the network property profiles toward the left tail of the histograms were substantially altered by global signal deconvolution, some connections were consistently observed in the negative-most tail networks both with and without global signal removal. These tended to be long-range links, with edges between the supramarginal gyrus and both

the frontal medial orbital cortex and the posterior cingulate cortex present both with and without global signal regression and across a range of costs and thresholds in both equi-sparse and equi-threshold networks. This suggests that these links represent the consistently weakest correlations in the network, attaining a strongly negative valence only when global signal removal was employed.

Using the magnitude of the correlation coefficient to construct networks will thus mix different topologies associated with the right and left tails of the histogram. The impact was greatest with global signal removal as the negative tails were mapped across to similar positive values and the resulting network parameters were compromised.

#### Reproducibility of network parameters

Although the within-subject reproducibility of independent component analysis and seed-region based analyses of resting state connectivity has been assessed (Zuo et al., 2010a,b; Shehzad et al., 2009), that of graph theoretic measures of resting brain connectivity has received less attention. Deuker et al. (2009) demonstrated robust reproducibility of MEG-derived graph-theoretic measures during a working memory task (but less so during rest). Interestingly, for all preprocessing strategies, we found that equi-threshold binary networks had systematically higher within-subject reproducibility than corresponding equi-sparse networks. This is consistent with the good within-subject reproducibility observed for the correlation histograms, but seemingly in contrast to the reduced between-subject variability in network parameters achieved with equi-sparse networks (Hayasaka and Laurienti, 2010), and suggests

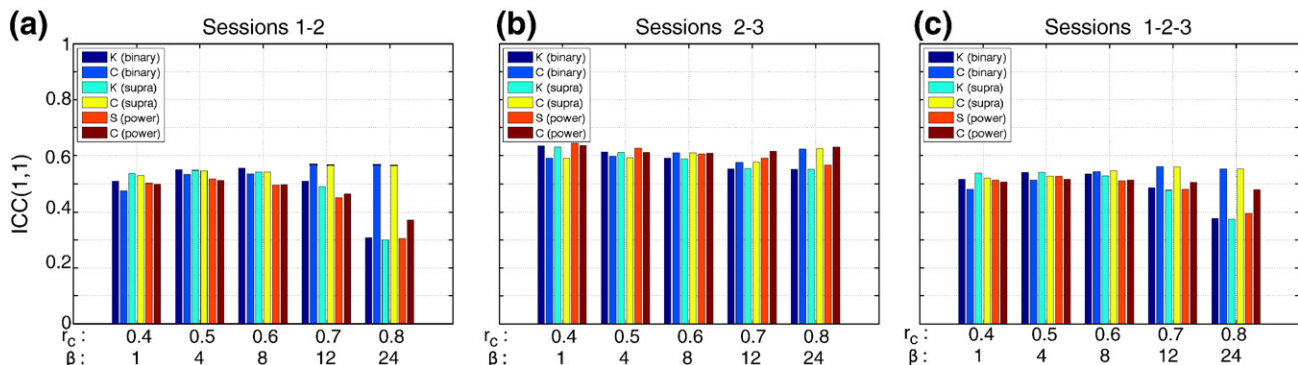


**Fig. 8.** ICC values for global (network average) parameters node strength ( $S$ , or degree  $K$ ) and clustering coefficient ( $C$ ) derived from hard-thresholded (binary, supra-threshold) and soft-thresholded (power adjacency function) networks over a range of thresholds ( $r_c$ ) or parameter values ( $\beta$ ). (a) Sessions 1 and 2, (b) sessions 2 and 3, and (c) all three scanning sessions.



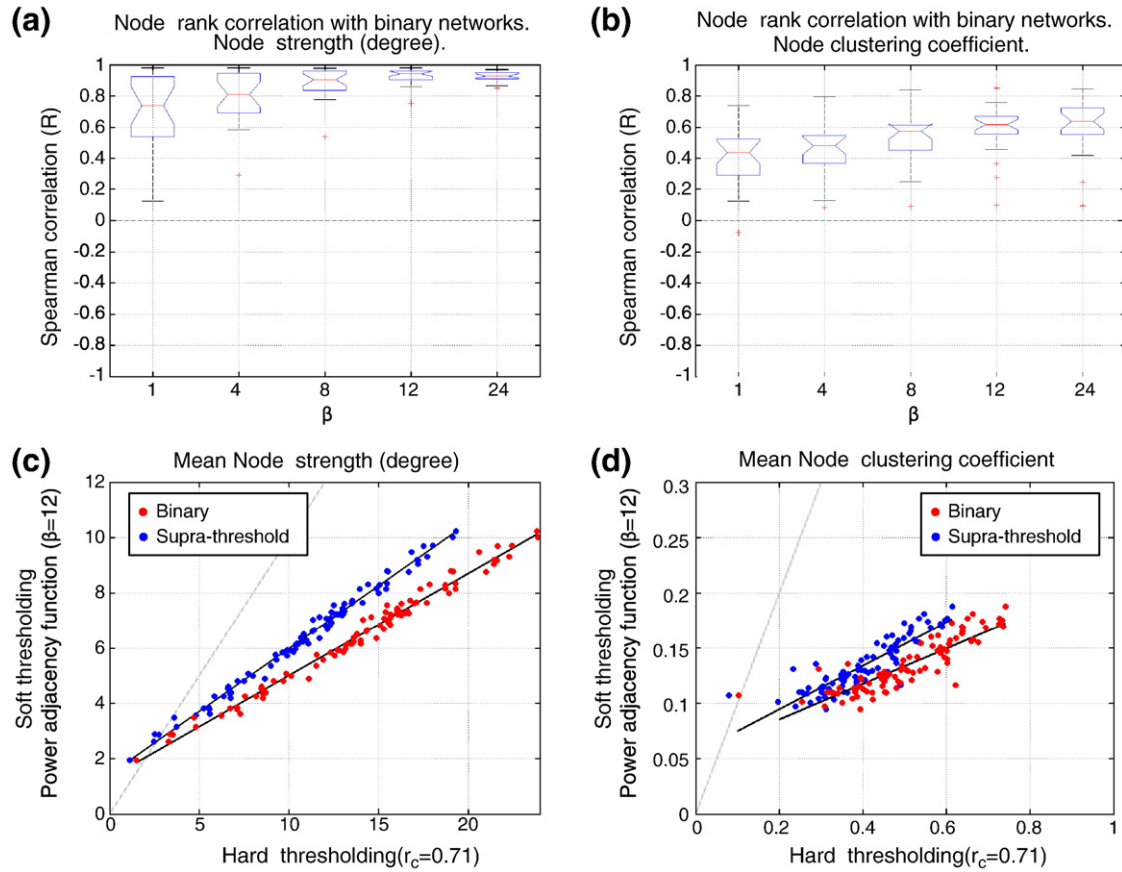


**Fig. 9.** Correspondence between node strength (degree) and clustering coefficient in soft-thresholded and hard-thresholded networks (equi-threshold,  $r_c > 0.71$ ). (a) Spearman rank correlation across nodes between  $s_i$  in soft-thresholded networks ( $\beta \in \{1, 4, 8, 12, 24\}$ ) and  $k_i$  in binary networks. Boxplots represent median, 25th and 75th quartiles and range. (b) Spearman rank correlation across nodes between  $c_i$  in soft-thresholded ( $\beta \in \{1, 4, 8, 12, 24\}$ ) and binary networks. Boxplots represent median, 25th and 75th quartiles and range. (c) Plot of mean  $s_i$  vs.  $k_i$  across subjects, for each node, for soft-thresholded networks ( $\beta = 12$ ) versus both binary (red) and supra-threshold (blue) networks. (d) Plot of mean  $c_i$  across subjects, for each node, for soft-thresholded networks ( $\beta = 12$ ) versus both binary (red) and supra-threshold (blue) networks.

that the numeric values of the inter-node correlations, and hence the derived network parameters, were to some degree preserved across repeated scanning sessions.

#### Fully weighted and soft-thresholded networks

The above findings supported the choice of power law adjacency functions as described in Eq. (4), with a fixed mapping of correlation coefficient  $r_{ij}$  to edge weight  $w_{ij}$ . This in fact provides a flexible set of mappings, from a simple linear transformation with  $\beta = 1$  to increasingly

non-linear transformations with  $\beta > 1$  that enable the properties of the positive-most tail of the similarity measure distribution to be emphasized without complete edge removal and hence avoiding issues related to fragmentation of the adjacency matrix. Given that global signal removal altered the topological characteristics and did not improve reproducibility of positive-tail network parameters, we investigated soft-thresholded networks using data preprocessed with white matter, CSF and head motion signal deconvolution. This preprocessing scheme yielded the highest overall reproducibility while accounting for possible confounding effects from these three sources.

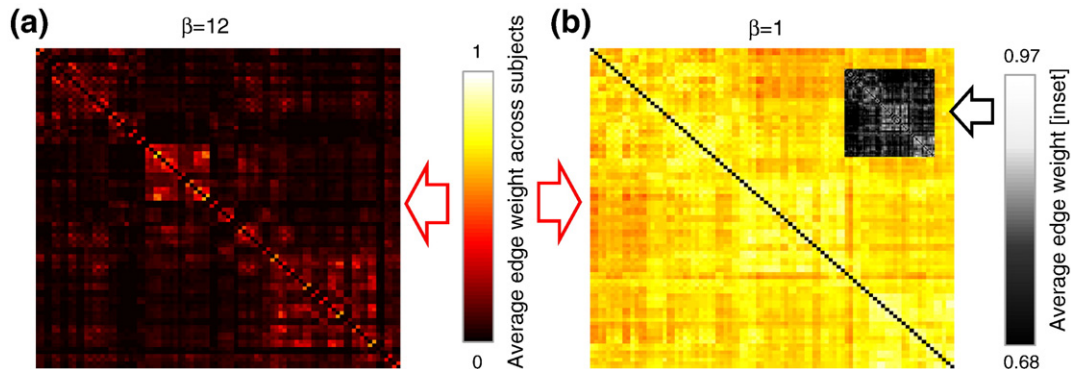


**Fig. 10.** Average edge weight across subjects of soft-thresholded networks, with nodes ordered according to the positive-tail networks in Fig. 4. Network (a), constructed with  $\beta = 12$ , shows a similar modular structure as the binary network in Fig. 4(c). Network (b), constructed using a linear adjacency transformation ( $\beta = 1$ ), shows a reduced dynamic range in mean edge weight although modular structure is present (inset: windowed between 25th percentile (0.68) and maximum (0.97) group-mean edge weights).

We found that soft-thresholded networks yielded reproducible network parameters over a range of  $\beta$ , with ICC values  $\sim 0.5 - 0.6$  and very similar to those obtained with hard-thresholded networks over a range of threshold values. As expected, reproducibility between scans obtained in the same day (sessions 2–3) was higher than between those obtained 5–16 months apart (sessions 1–2). Moreover, node-wise clustering coefficient and strength parameter values computed from soft-thresholded networks showed a strong correspondence with parameters computed from hard-thresholded versions of the networks. The dynamic range of these parameter values was compressed in the soft-thresholded networks due to the retention of low, but non-zero, edge weights. Soft-thresholded networks also retained a modular structure, even in the linear limit  $\beta = 1$ , although in the latter case the edge weight distribution remained substantially right-shifted and hence compressed in dynamic range (see Fig. 6). Recently, Mumford et al., (2010) also demonstrated a robust modular decomposition of soft-thresholded networks at the voxel scale using a power law adjacency function.

Although the soft-thresholding approach removes the issue of selecting an absolute, hard threshold, the need to select a parameter value for the adjacency function remains. The power law mapping used in the present study allows the original correlation matrix to be faithfully reflected in the final edge weights in the linear limit ( $\beta = 1$ ), or for the characteristics associated with the strongest correlation values to be progressively emphasized with increasing  $\beta > 1$ . In the present study, we found that the edge weight distribution approached a profile similar to the (truncated) power law observed with binary networks, and evidenced highly-clustered “small-world” properties, at parameter values of  $\beta \geq 12$ . Reproducibility of node strength and clustering coefficient, however, began to drop off slightly at  $\beta \geq 12$ . These suggest that in the absence of global signal removal a value  $\beta \sim 12$  may be a good choice to capture these non-random ‘right tail’ network properties whilst retaining reproducibility. Indeed, Mumford et al. (2010), removing motion traces but not the global signal, applied a scale-free fit criterion (Zhang and Horvath, 2005) to select values of  $\beta$  individually for each network, a process that yielded a mean value of  $\beta = 12.4$  across networks in that study. Due to the potential variability, and occasional non-monotonic nature, of the curves generated using this approach, in the present study we evaluated applying a consistent value of  $\beta$  to all networks, but reached a similar conclusion regarding an appropriate choice of soft-thresholding parameter. (The behavior of soft-thresholded networks with global signal removal was consistent with the fact that the similarity histograms were zero-centered, with lower parameter values ( $\beta \geq 8$ ) sufficient to capture small-world behavior and low node strength dominance in the network (see Supplemental Data).)

An argument against the use of complete, weighted networks is that low edge weights may convey more noise than signal and potentially obscure the distinct network topology observed at higher edge weights (Rubinov and Sporns, 2010). This is consistent with the observation of binary network properties that approach those of random networks as the threshold is relaxed (Van den Heuvel et al., 2008) as well as the properties observed at intermediate correlation values in the present study (Fig. 3). On the other hand, disease or intervention may give rise to systematic (across subjects) shifts in correlation strength that may be distorted or missed entirely by hard-thresholding approaches. Further studies using soft-thresholding approaches in the context of network modulation by disease state, intervention (Lohmann et al., 2010) or pharmacological treatment, will also help inform on the value of weighted networks from the viewpoint of sensitivity to a perturbation to the system.

In this study, we mapped correlation coefficients into the range  $[0, 1]$  to explore continuous generalizations of graph theoretic parameters and for comparison with hard-thresholded networks whose edges fall within the same range. Mappings retaining the edge valence, resulting in signed networks, can also be constructed; most

simply, the original correlation coefficients can be retained as edge weights  $w_{ij} = r_{ij}$  in a variation on the linear ( $\beta = 1$ ) transformation. The present study suggests that the impact of this would be strongest if global signal removal is employed.

#### Choice of similarity measure

Network connections or edge weights are also dependent on the choice of similarity measure used to quantify the relationship between the time courses in the different brain regions. In the present study we employed the (zero-lag) Pearson linear correlation coefficient. This has been a popular choice in studies of brain functional connectivity networks (Van den Heuvel et al., 2008, 2009a; Hayasaka and Laurienti, 2010; Wang et al., 2010b). However, other similarity measures have also been used, including correlation between wavelet components (Achard et al., 2006; Achard and Bullmore, 2007; Meunier et al., 2009b) the partial correlation coefficient (Salvador et al., 2005a; Liu et al., 2008; Nakamura et al., 2009; Wang et al., 2010b), and mutual information (Salvador et al., 2005b). The adjacency function can be easily reformulated for similarity measures of different intrinsic arithmetic range. In general, the choice of similarity measure and the manner in which this choice affects graph theoretic properties is another important variable (Smith et al., 2011).

#### Spatial scale

An important limitation of soft-thresholding approaches is the computational resource required to calculate network parameters in complete networks, in which all possible connections are present, albeit with differing edge weights. For this reason, in the present study we profiled the soft-thresholding properties using small ( $N_{\text{node}} = 90$ ) networks derived from an atlas-based parcellation of the cortical and sub-cortical regions of the brain. The automated anatomical labelling (AAL) atlas employed (Tzourio-Mazoyer et al., 2002) has been a popular choice in network analyses (Achard et al., 2006; Achard and Bullmore, 2007; Liu et al., 2008; Wang et al., 2010b) but provides a relatively coarse parcellation, the results of which may be atlas-dependent (Wang et al., 2009) and not optimally represent underlying functional units. For binary networks, atlas-based parcellations may be limited in the extent to which they approximate the properties observed at finer parcellations (Hayasaka and Laurienti, 2010; Fornito et al., 2010) and more prone to disconnection (Fornito et al., 2010). Networks derived from brain regions defined from small functional units or at fully voxel-scale (‘mesoscopic’) spatial resolution have begun to be investigated in the case of binary thresholding (Schwarz et al., 2009; Meunier et al., 2009b; Hayasaka and Laurienti, 2010; Schwarz et al., 2010; Fornito et al., 2010). Nevertheless, the network properties demonstrated in the present study provide specific hypotheses to be addressed as these concepts are extended to higher spatial-resolution networks.

#### Conclusions

Functional connectivity networks created from the left tail of the correlation histogram had topological properties distinct from the familiar right-tail networks. In the absence of global signal correction, left-tail networks comprised predominantly long-range connections associated with weak correlations and were characterized by substantially reduced values of modularity and the clustering coefficient, negative assortativity and small-world parameter ( $\sigma_{\text{sw}} < 1$ ). Following global signal removal, where stronger anti-correlations are present, network parameters were altered in the left tail in particular, with clustering coefficient and assortativity associated with negative edges converging to zero. Deconvolution of white matter, CSF and motion signals yielded the greatest within-subject reproducibility of

network parameters (ICC(1,1) values  $\sim 0.5$ ). Soft-thresholding using a power law adjacency function with  $\beta \sim 12$  yielded modular networks with parameters that agreed well with corresponding hard-thresholded values, were reproducible in repeated sessions across many months, and evidenced small-world-like (elevated clustering) and scale-free-like (node strength distributions characterized by a truncated power law). Fully-weighted networks created using a linear transformation retained a modular structure only.

## Appendix A. Supplementary data

Supplementary data to this article can be found online at doi:10.1016/j.neuroimage.2010.12.047.

## References

- Achard, S., Bullmore, E., 2007. Efficiency and cost of economical brain functional networks. *PLoS Comput. Biol.* 3 (2), e17.
- Achard, S., Salvador, R., Whitcher, B., Suckling, J., Bullmore, E., 2006. A resilient, low-frequency, small-world human brain functional network with highly connected association cortical hubs. *J. Neurosci.* 26 (1), 63–72.
- Almaas, E., 2007. Biological impacts and context of network theory. *J. Exp. Biol.* 210 (9), 1548.
- Andrews-Hanna, J., Snyder, A., Vincent, J., Lustig, C., Head, D., Raichle, M., Buckner, R., 2007. Disruption of large-scale brain systems in advanced aging. *Neuron* 56 (5), 924–935.
- Baliki, M., Geha, P., Apkarian, A., Chialvo, D., 2008. Beyond feeling: chronic pain hurts the brain, disrupting the default-mode network dynamics. *J. Neurosci.* 28 (6), 1398.
- Bassett, D., Bullmore, E., 2006. Small-world brain networks. *Neuroscientist* 12 (6), 512.
- Bassett, D., Bullmore, E., Verchinski, B., Mattay, V., Weinberger, D., Meyer-Lindenberg, A., 2008. Hierarchical organization of human cortical networks in health and schizophrenia. *J. Neurosci.* 28 (37), 9239.
- Beckmann, C., DeLuca, M., Devlin, J., Smith, S., 2005. Investigations into resting-state connectivity using independent component analysis. *Philos. Trans. R. Soc. B Biol. Sci.* 360 (1457), 1001.
- Birn, R., Diamond, J., Smith, M., Bandettini, P., 2006. Separating respiratory-variation-related fluctuations from neuronal-activity-related fluctuations in fMRI. *Neuroimage* 31 (4), 1536–1548.
- Biswal, B., Yetkin, F., Haughton, V., Hyde, J., 1995. Functional connectivity in the motor cortex of resting human brain using echo-planar MRI. *Magn. Reson. Med.* 34 (4), 537–541.
- Braun, R., Wilson, R., Pelesko, J., Buchanan, J., Gleeson, J., 2006. Applications of small-world network theory in alcohol epidemiology. *J. Stud. Alcohol* 67 (4), 591.
- Buckner, R., Sepulcre, J., Talukdar, T., Krienen, F., Liu, H., Hedden, T., Andrews-Hanna, J., Sperling, R., Johnson, K., 2009. Cortical hubs revealed by intrinsic functional connectivity: mapping, assessment of stability, and relation to Alzheimer's disease. *J. Neurosci.* 29 (6), 1860.
- Bullmore, E., Sporns, O., 2009. Complex brain networks: graph theoretical analysis of structural and functional systems. *Nat. Rev. Neurosci.* 10 (3), 186–198.
- Chang, C., Glover, G., 2009. Effects of model-based physiological noise correction on default mode network anti-correlations and correlations. *Neuroimage* 47 (4), 1448–1459.
- Chang, C., Glover, G., 2010. Time-frequency dynamics of resting-state brain connectivity measured with fMRI. *Neuroimage* 50 (1), 81–98.
- Christley, R., French, N., 2003. Small-world topology of UK racing: the potential for rapid spread of infectious agents. *Equine Vet. J.* 35 (6), 586–589.
- Deuker, L., Bullmore, E., Smith, M., Christensen, S., Nathan, P., Rockstroh, B., Bassett, D., 2009. Reproducibility of graph metrics of human brain functional networks. *Neuroimage* 47 (4), 1460–1468.
- Eguiluz, V., Chialvo, D., Cecchi, G., Baliki, M., Apkarian, A., 2005. Scale-free brain functional networks. *Phys. Rev. Lett.* 94 (1), 18102.
- Ferrarini, L., Veer, I., Baerends, E., van Tol, M., Renken, R., van der Wee, N., Veltman, D., Aleman, A., Zitman, F., Penninx, B., et al., 2009. Hierarchical functional modularity in the resting-state human brain. *Hum. Brain Mapp.* 30 (7), 2220–2231.
- Fornito, A., Zalesky, A., Bullmore, E., 2010. Network scaling effects in graph analytic studies of human resting-state fMRI data. *Front. Syst. Neurosci.* 4, 22.
- Fox, M., Raichle, M., 2007. Spontaneous fluctuations in brain activity observed with functional magnetic resonance imaging. *Nat. Rev. Neurosci.* 8 (9), 700–711.
- Fox, M., Zhang, D., Snyder, A., Raichle, M., 2009. The global signal and observed anti-correlated resting state brain networks. *J. Neurophysiol.* 101 (6), 3270.
- Glover, G., Li, T., Ress, D., 2000. Image-based method for retrospective correction of physiological motion effects in fMRI: RETROICOR. *Magn. Reson. Med.* 44 (1), 162–167.
- Greicius, M., 2008. Resting-state functional connectivity in neuropsychiatric disorders. *Curr. Opin. Neurol.* 21 (4), 424.
- Greicius, M., Srivastava, G., Reiss, A., Menon, V., 2004. Default-mode network activity distinguishes Alzheimer's disease from healthy aging: evidence from functional MRI. *Proc. Natl. Acad. Sci.* 101 (13), 4637.
- Hayasaka, S., Laurienti, P., 2010. Comparison of characteristics between region- and voxel-based network analyses in resting-state fMRI data. *Neuroimage* 50, 499–508.
- He, Y., Wang, J., Wang, L., Chen, Z., Yan, C., Yang, H., Tang, H., Zhu, C., Gong, Q., Zang, Y., et al., 2009. Uncovering intrinsic modular organization of spontaneous brain activity in humans. *PLoS ONE* 4 (4), e5226.
- Holten, D., 2006. Hierarchical edge bundles: visualization of adjacency relations in hierarchical data. *IEEE Trans. Vis. Comput. Graph.* 12 (6), 741–748.
- Jo, H., Saad, Z., Simmons, W., Milbury, L., Cox, R., 2010. Mapping sources of correlation in resting state fMRI, with artifact detection and removal. *Neuroimage* 52 (2), 571–582.
- Kelly, C., de Zubicaray, G., Di Martino, A., Copland, D., Reiss, P., Klein, D., Castellanos, F., Milham, M., McMahon, K., 2009. L-dopa modulates functional connectivity in striatal cognitive and motor networks: a double-blind placebo-controlled study. *J. Neurosci.* 29 (22), 7364.
- Liu, Y., Liang, M., Zhou, Y., He, Y., Hao, Y., Song, M., Yu, C., Liu, H., Liu, Z., Jiang, T., 2008. Disrupted small-world networks in schizophrenia. *Brain* 131 (4), 945.
- Lohmann, G., Margulies, D., Horstmann, A., Pleger, B., Lepsien, J., Goldhahn, D., Schloegl, H., Stumvoll, M., Villringer, A., Turner, R., 2010. Eigenvector centrality mapping for analyzing connectivity patterns in fMRI data of the human brain. *PLoS ONE* 5 (4), e10232.
- Mantini, D., Perrucci, M., Del Gratta, C., Romani, G., Corbetta, M., 2007. Electrophysiological signatures of resting state networks in the human brain. *Proc. Natl. Acad. Sci.* 104 (32), 13170.
- Maslov, S., Sneppen, K., 2002. Specificity and stability in topology of protein networks. *Science* 296 (5569), 910.
- McGonigle, J., Mirmehdi, M., Malizia, A., 2011. Visualising functional connectivity in fMRI using hierarchical edge bundles. 17th Annual Meeting of the Organization for Human Brain Mapping, June 2011, Quebec City.
- McGraw, K., Wong, S., 1996. Forming inferences about some intraclass correlation coefficients. *Psychol. Meth.* 1 (1), 30–46.
- Meunier, D., Achard, S., Morcom, A., Bullmore, E., 2009a. Age-related changes in modular organization of human brain functional networks. *Neuroimage* 44 (3), 715–723.
- Meunier, D., Lambiotte, R., Fornito, A., Ersche, K., Bullmore, E., 2009b. Hierarchical modularity in human brain functional networks. *Front. Neuroinformatics* 3, 37.
- Mumford, J., Horvath, S., Oldham, M., Langfelder, P., Geschwind, D., Poldrack, R., 2010. Detecting network modules in fMRI time series: a weighted network analysis approach. *Neuroimage* 52 (4), 1456–1476.
- Murphy, K., Birn, R., Handwerker, D., Jones, T., Bandettini, P., 2009. The impact of global signal regression on resting state correlations: are anti-correlated networks introduced? *Neuroimage* 44 (3), 893–905.
- Nakamura, T., Hillary, F., Biswal, B., 2009. Resting network plasticity following brain injury. *PLoS ONE* 4 (12), e8220.
- Reijneveld, J., Ponten, S., Berendse, H., Stam, C., 2007. The application of graph theoretical analysis to complex networks in the brain. *Clin. Neurophysiol.* 118 (11), 2317–2331.
- Rubinov, M., Sporns, O., 2010. Complex network measures of brain connectivity: uses and interpretations. *Neuroimage* 52 (3), 1059–1069.
- Salvador, R., Suckling, J., Coleman, M., Pickard, J., Menon, D., Bullmore, E., 2005a. Neurophysiological architecture of functional magnetic resonance images of human brain. *Cereb. Cortex* 15 (9), 1332.
- Salvador, R., Suckling, J., Schwarzbauer, C., Bullmore, E., 2005b. Undirected graphs of frequency-dependent functional connectivity in whole brain networks. *Philos. Trans. R. Soc. B Biol. Sci.* 360 (1457), 937.
- Schölvinck, M., Maier, A., Ye, F., Duyn, J., Leopold, D., 2010. Neural basis of global resting-state fMRI activity. *Proc. Natl. Acad. Sci.* 107 (22), 10238.
- Schwarz, A., Gozzi, A., Bifone, A., 2009. Community structure in networks of functional connectivity: resolving functional organization in the rat brain with pharmacological MRI. *Neuroimage* 47 (1), 302–311.
- Schwarz, A., Upadhyay, J., Coimbra, A., Baumgartner, R., Anderson, J., Bishop, J., George, E., Becerra, L., Borsook, D., 2010. Mapping threshold-independent drug effects in graph theoretic analyses of functional connectivity networks: the opioid analgesic buprenorphine preferentially modulates network topology in pain-processing regions. *Proc. ISMRM* 18, 432.
- Shehzad, Z., Kelly, A., Reiss, P., Gee, D., Gotimer, K., Uddin, L., Lee, S., Margulies, D., Roy, A., Biswal, B., et al., 2009. The resting brain: unconstrained yet reliable. *Cereb. Cortex* 19 (10), 2209–2229.
- Shen, X., Papademetris, X., Constable, R., 2010. Graph-theory based parcellation of functional subunits in the brain from resting-state fMRI data. *Neuroimage* 50 (3), 1027–1035.
- Shmueli, K., van Gelderen, P., de Zwart, J., Horovitz, S., Fukunaga, M., Jansma, J., Duyn, J., 2007. Low-frequency fluctuations in the cardiac rate as a source of variance in the resting-state fMRI BOLD signal. *Neuroimage* 38 (2), 306–320.
- Shrout, P., Fleiss, J., 1979. Intraclass correlations: uses in assessing rater reliability. *Psychol. Bull.* 86 (2), 420–428.
- Sienkiewicz, J., Holyst, J., 2005. Statistical analysis of 22 public transport networks in Poland. *Phys. Rev. E* 72 (4), 46127.
- Smith, S., Miller, K., Salimi-Khorshidi, G., Webster, M., Beckmann, C., Nichols, T., Ramsey, J., Woolrich, M., 2011. Network modelling methods for FMRI. *Neuroimage* 54 (2), 875–891.
- Stam, C., Reijneveld, J., 2007. Graph theoretical analysis of complex networks in the brain. *Nonlinear Biomed. Phys.* 1 (1), 3.
- Tzourio-Mazoyer, N., Landeau, B., Papathanassiou, D., Crivello, F., Etard, O., Delcroix, N., Mazoyer, B., Joliot, M., 2002. Automated anatomical labeling of activations in SPM using a macroscopic anatomical parcellation of the MNI MRI single-subject brain. *Neuroimage* 15 (1), 273–289.
- Valencia, M., Pastor, M., Fernández-Seara, M., Artieda, J., Martinier, J., Chavez, M., 2009. Complex modular structure of large-scale brain networks. *Chaos: an interdisciplinary J. Nonlinear Sci.* 19, 023119.



- van den Heuvel, M., Mandl, R., Kahn, R., Pol, H., 2009a. Functionally linked resting-state networks reflect the underlying structural connectivity architecture of the human brain. *Hum. Brain Mapp.* 30 (10), 3127–3141.
- Van den Heuvel, M., Stam, C., Boersma, M., Hulshoff Pol, H., 2008. Small-world and scale-free organization of voxel-based resting-state functional connectivity in the human brain. *Neuroimage* 43 (3), 528–539.
- van den Heuvel, M., Stam, C., Kahn, R., Hulshoff Pol, H., 2009b. Efficiency of functional brain networks and intellectual performance. *J. Neurosci.* 29 (23), 7619.
- Vendruscolo, M., Dokholyan, N., Paci, E., Karplus, M., 2002. Small-world view of the amino acids that play a key role in protein folding. *Phys. Rev. E* 65 (6), 61910.
- Vincent, J., Snyder, A., Fox, M., Shannon, B., Andrews, J., Raichle, M., Buckner, R., 2006. Coherent spontaneous activity identifies a hippocampal–parietal memory network. *J. Neurophysiol.* 96 (6), 3517.
- Wagner, A., Fell, D., 2001. The small world inside large metabolic networks. *Proc. R. Soc. Lond. B Biol. Sci.* 268 (1478), 1803.
- Wang, J., Wang, L., Zang, Y., Yang, H., Tang, H., Gong, Q., Chen, Z., Zhu, C., He, Y., 2009. Parcellation-dependent small-world brain functional networks: a resting-state fMRI study. *Hum. Brain Mapp.* 30 (5), 1511–1523.
- Wang, J., Zuo, X., He, Y., 2010a. Graph-based network analysis of resting-state functional MRI. *Front. Syst. Neurosci.* 4 (16). doi:10.3389/fnsys.2010.00016.
- Wang, L., Li, Y., Metzack, P., He, Y., Woodward, T., 2010b. Age-related changes in topological patterns of large-scale brain functional networks during memory encoding and recognition. *Neuroimage* 50 (3), 862–872.
- Watts, D., Strogatz, S., 1998. Collective dynamics of small-world networks. *Nature* 393 (6684), 440–442.
- Whitfield-Gabrieli, S., Thermenos, H., Milanovic, S., Tsuang, M., Faraone, S., McCarley, R., Shenton, M., Green, A., Nieto-Castanon, A., LaViolette, P., et al., 2009. Hyperactivity and hyperconnectivity of the default network in schizophrenia and in first-degree relatives of persons with schizophrenia. *Proc. Natl Acad. Sci.* 106 (4), 1279.
- Wu, T., Wang, L., Chen, Y., Zhao, C., Li, K., Chan, P., 2009. Changes of functional connectivity of the motor network in the resting state in Parkinson's disease. *Neurosci. Lett.* 460 (1), 6–10.
- Zhang, B., Horvath, S., 2005. A general framework for weighted gene co-expression network analysis. *Stat. Appl. Genet. Mol. Biol.* 4 (1), 1128.
- Zuo, X., Di Martino, A., Kelly, C., Shehzad, Z., Gee, D., Klein, D., Castellanos, F., Biswal, B., Milham, M., 2010a. The oscillating brain: complex and reliable. *Neuroimage* 49 (2), 1432–1445.
- Zuo, X., Kelly, C., Adelstein, J., Klein, D., Castellanos, F., Milham, M., 2010b. Reliable intrinsic connectivity networks: test–retest evaluation using ICA and dual regression approach. *Neuroimage* 49 (3), 2163–2177.